Kv4.3 channel downregulation mediates chronic post-lesional pacemaker acceleration in surviving dopamine substantia nigra neurons

Lora Kovacheva[1], Josef Shin, Navid Farassat[*] & Jochen Roeper[1]

Institute of Neurophysiology, Neuroscience Center, Goethe University, Frankfurt, Germany.

*Present address: Eye Center, Medical Center, Medical Faculty, Albert-Ludwig University Freiburg, Germany

[1] Corresponding authors:

Prof. Dr. Jochen Roeper & Lora Kovacheva

Institute for Neurophysiology

Neuroscience Center, Goethe University

Theodor-Stern-Kai 7, 60590 Frankfurt, Germany

e-mail: roeper@em.uni-frankfurt.de & email: lorask@gmail.com

Tel: +49-69-6301-84091/92

Abstract

Substantia nigra dopamine (SN DA) neurons are progressively lost in Parkinson disease (PD). While the molecular and cellular mechanisms of their differential vulnerability and degeneration have been extensively studied, we still know very little about potential functional adaptations of those SN DA neurons that – at least for some time – manage to survive during earlier stages of PD. We utilized a partial lesion 6-OHDA mouse model to characterize initial electrophysiological impairments and chronic adaptations of surviving identified SN DA neurons, both *in vivo* and *in vitro*. Early after lesion (3 weeks), we detected a selective loss of *in vivo* burst firing in surviving SN DA neurons, which was accompanied by *in vitro* pacemaker instability. In contrast, late after lesion (>2 months), *in vivo* firing properties of surviving SN DA neurons had recovered in the presence of 2-fold accelerated pacemaking *in vitro*. Finally, we show that this chronic cell-autonomous adaptation in surviving SN DA neurons was mediated by Kv4.3 channel downregulation. Our study demonstrates substantial homeostatic plasticity of surviving SN DA neurons after a single-hit non-progressive lesion, which might contribute to the phenotype of initially surviving SN DA neurons in PD.

Keywords

dopamine, 6-OHDA, Kv4.3 channel, substantia nigra, accelerated pacemaker

38 ## Introduction

39

40 One clinically relevant hallmark of Parkinson disease (PD) is the progressive degeneration of
41 vulnerable neuronal populations, including substantia nigra dopamine (SN DA) neurons (Giguere et
42 al., 2018; Kalia and Lang, 2015; Poewe et al., 2017). At the time of clinical diagnosis, more than 50%
43 of SN DA neurons, in particular those in ventrolateral regions, are already lost (Gibb and Lees, 1991;
44 Kordower et al., 2013). Moreover, Kordower and colleagues (Kordower *et al.*, 2013) demonstrated
45 that most remaining SN DA neurons were rapidly lost (or lose their DA phenotype) within the first few
46 years of clinically manifest PD. While neuropathological studies map the time course of degeneration
47 with cellular resolution and also allow for a molecular characterization of the remaining neurons, they
48 cannot investigate the functional properties of surviving neurons. *In vivo* recordings of putative human
49 SN DA neurons in the context of DBS surgery provided a first glimpse of electrically active DA survivors
50 (Dragicevic et al., 2015; Schiemann et al., 2012; Zaghloul et al., 2009), but a systematic investigation
51 of these DA neurons is not feasible in a therapeutic setting. Thus, studying functional adaptations of
52 surviving DA neurons in the context of PD is the domain of animal models, which themselves often
53 capture only partial aspects of the disease. Among the various rodent PD models, 6-hydroxydopamine
54 (6-OHDA) lesions have been extensively used to study the DA-depleted basal ganglia (Chen et al., 2021;
55 Fieblinger et al., 2018; Kravitz et al., 2010; Parker et al., 2018; Parker et al., 2016; Rubi and Fritschy,
56 2020; Sharott et al., 2005; Sitzia et al., 2020; Ungerstedt, 1968; West et al., 2018). By comparison, a
57 smaller number of studies applying only partial lesions focused on the properties of the remaining DA
58 midbrain system, including its long-term adaptations and drug responses (Bez et al., 2016). These
59 studies demonstrated that – in contrast to PD – 6-OHDA DA lesions are non-progressive (i.e. single-
60 hit) and follow a stereotypical time course: an initial phase dominated by cell loss, inflammation and
61 behavioral impairment for about 3 weeks, which is followed by a chronic phase (studied for up to 20
62 month in mice), where partial behavioral recovery, neurochemical and molecular adaptations and –
63 to a certain degree – axonal sprouting of DA neurons occur (Bez *et al.*, 2016; Cenci and Bjorklund,
64 2020; Kirik et al., 1998; Schwarting and Huston, 1996; Winkler et al., 2002). Single cell

electrophysiological investigations of viable post-lesional DA neurons, however, have been exceedingly rare with only Hollerman & Grace providing a first data set (Hollerman and Grace, 1990). They found 6-0HDA-lesion-size-dependent changes in *in vivo* firing properties of putative DA neurons in rats, among them a decrease of *in vivo* burst firing after 50-60% (sized) lesions (Hollerman and Grace, 1990).

In contrast, cell-autonomous characteristics of surviving SN DA neurons after 6-OHDA lesion have not yet been studied. Here, we aim to close this gap by exploring the electrophysiological properties *in vivo* and *in vitro* of surviving SN DA neurons in a well-characterized, intra-striatal unilateral 6-OHDA lesion mouse model, where about 50% of SN DA neurons survive. We selected two time points of electrophysiological investigation based on our long-term behavioral characterization of motor phenotypes. In particular, we studied the dynamics of spontaneous locomotion and turning behavior in a drug-free setting. This identified a 3-week post-lesion time point (i.e. early phase), where motor impairment was prominent, and a stable late phase (>68 days post-lesion), where turning asymmetry had completely recovered. In contrast to the significant behavioral differences between early and late post-lesional time points, the extent of the striatal lesion and the degree of stereologically-determined TH-positive cell numbers were stable. This pointed to a relevant contribution of early functional impairment and late adaptation in a stable pool of surviving SN DA neurons as detailed below.

83 ## Results

84

85 ### Early behavioral impairments and long-term adaptations after partial lesion of substantia nigra
86 dopamine neurons

87

88 In order to identify potential compensatory adaptations in surviving SN DA neurons, we utilized a
89 C57Bl6N mouse model with a partial 6-OHDA lesion of the nigrostriatal pathway. The neurotoxin 6-
90 OHDA was unilaterally infused into the right dorsal striatum, causing a partial degeneration of DA
91 neurons in the ipsilateral substantia nigra, which was quantified by unbiased stereology (Fig. 1A). We
92 continuously characterized motor behavior of the model (i.e. open field, cylinder test) until two
93 different time points, either 21-days post-lesion (early phase) or more than 60 days post-lesion (late
94 phase). Initially, animals were sacrificed for TH immunohistochemistry in midbrain and striatum. As
95 shown in Fig. 1B, at the early phase, the number of TH-positive (i.e. dopaminergic) SN neurons was
96 reduced post-6-OHDA (lower left panels) compared to control mice, where only vehicle (ACSF with
97 ascorbic acid) was infused into the dorsal striatum (upper left panels). The right panel in Fig. 1B
98 displays the stereological results of TH-positive SN neurons for N=9 vehicle-treated and N=9 6-OHDA-
99 infused mice. The data were normalized to the stereological results of respective contralateral SN DA
100 neurons. In contrast to vehicle, where no ipsilateral loss of SN DA neurons was detected, the number
101 of ipsilateral surviving SN DA neurons in the early post-6-OHDA phase was on average reduced to
102 about 40% (Fig. 1B; vehicle: 100 ± 2.644 %; 6-OHDA: 36.85 ± 3.463%; $p < 0.0001$, Mann-Whitney test).
103 We also carried out the unbiased stereology for TH-positive SN neurons in the late phase and detected
104 a similar degree of loss (Suppl. Fig. 1C, vehicle: 102.6 ± 7.9 %; 6-OHDA: 39.96 ± 3.7 %; $p = 0.0262$,
105 Mann-Whitney test). These results indicated that SN DA cell loss was stable throughout our
106 observation period of more than 2 months. In addition, we analyzed the axonal compartment of DA
107 midbrain neurons by determining striatal TH-optical densities, both in early and late phase (Suppl. Fig.
108 1). Similar to cell counts, we found an about 50% reduction of TH-immunosignal in the ipsilateral dorsal

striatum, both in early and late phase, whereas the ventral striatum was only mildly affected (ca. 20% reduction). In summary, our model induces a stable loss of SN DA neurons, associated with a stable reduction of striatal TH-immunoreactivity throughout the entire observation period. In other words, in accordance with previous chronic 6-OHDA studies (Bez *et al.*, 2016; Cenci and Bjorklund, 2020; Schwarting and Huston, 1996), this model showed no progression and is therefore suitable to study functional adaptations in a stable pool of surviving SN DA neurons.

Fig 1 C shows our continuous behavioral monitoring of unilateral 6-OHDA and vehicle-treated mice before and up to 68 days post-infusion. Based on previous studies (Cenci and Bjorklund, 2020; Schwarting and Huston, 1996), we focused on the dynamics of drug-free spontaneous turning behavior during open field locomotion (Fig. 1C, lefts panels). In contrast to vehicle-infused mice, which displayed a stable symmetric ratio (ca. 50%) of ipsi- to contral-lateral turning throughout the entire experiment, 6-OHDA-infused mice showed a dramatic shift to ipsilateral turning immediately after treatment (Figure 1C, right panel). Interestingly, ipsilateral turns occurred in long sequences of up to 40 individuals turns, a pattern not observed in controls (Suppl. Fig. 2). Importantly for this study, these turning sequences as well as the overall ipsilateral bias gradually but eventually completely recovered over 2-months post treatment (two-way-ANOVA, p-value across time $p<0.0001$, p-value across groups $p<0.0001$, significant difference between vehicle and 6-OHDA group till day 40, Šídák's multiple comparisons test). Analysis of turning features, such as diameter or velocity, revealed that the recovered contralateral turns were similar to turns performed by vehicle-treated mice (Suppl. Fig. 3). This could be indicative for a degree of functional recovery and/or functional compensation within the stable pool of surviving DA neurons. General locomotion, measured as performed track length per session, recovered in parallel to the turning bias (Suppl. Fig. 1). However, other motor behaviors, such as contralateral paw use during rearing in the cylinder test, did not show recovery throughout the experimental period (Fig. 1D) (21st post-infusion day: vehicle 38.5 ± 5.24%, 6-OHDA 5.73 ± 1.35%, $p < 0.0001$, Mann-Whitney test; 68th post-infusion day: vehicle 63.67± 6.6%, 6-OHDA 3.167 ± 1.8%, $p < 0.0001$, Mann-Whitney test), which is consistent with the partial but stable loss of SN DA neurons and reduction of dorsal striatal TH.

136 To investigate this model's homeostatic mechanisms from the perspective of the surviving SN DA
137 neurons, we performed *in vivo* extracellular recordings and *in vitro* whole-cell patch-clamp recordings
138 once within a period with strong turning bias, at the 21st day after lesion (early phase), and at a later
139 time point – after reaching stable baseline levels (late phase).

140

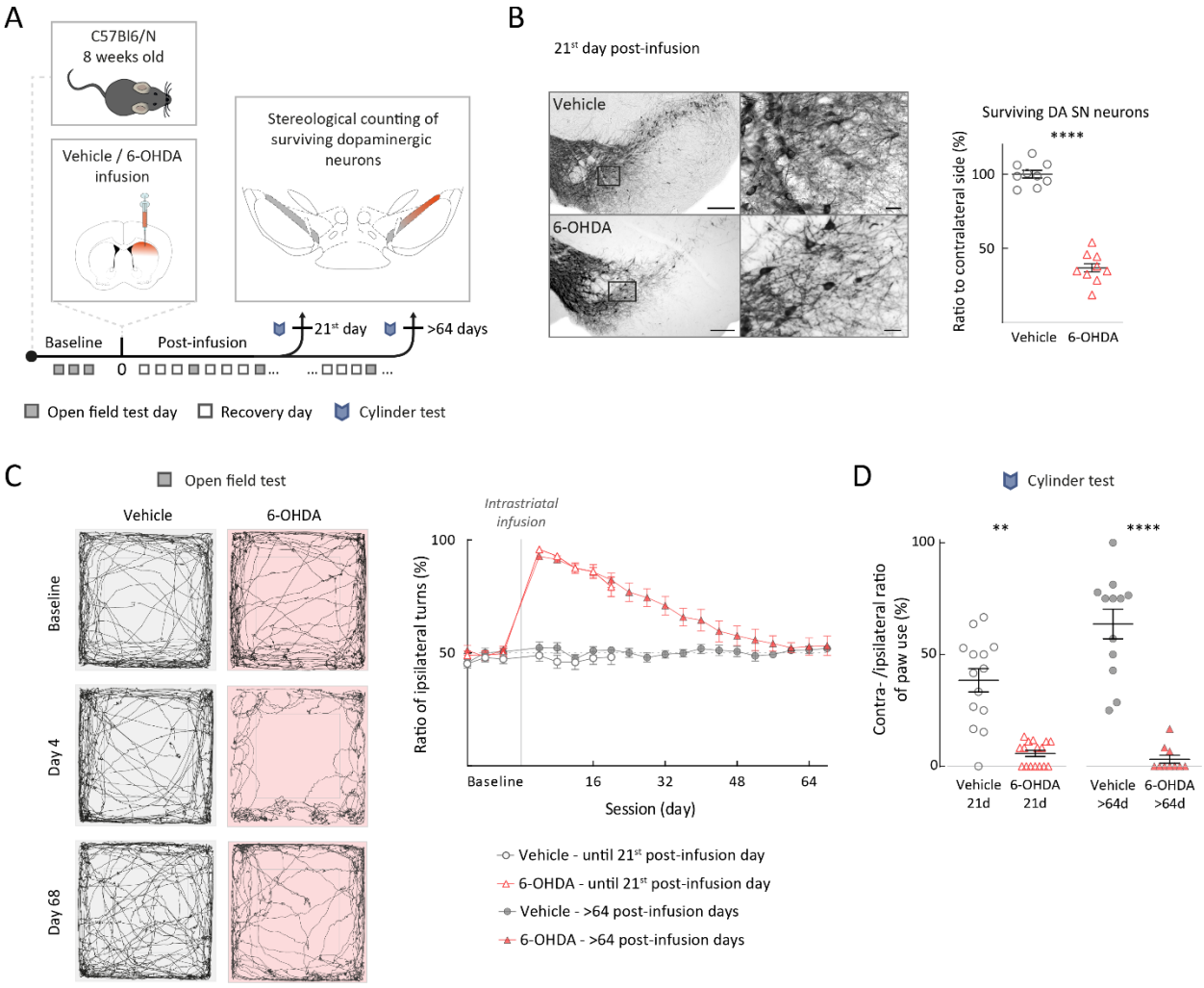

141

142 **Figure 1. Unilateral striatal 6-OHDA mouse model with stable loss of SN DA neurons resulted in**
143 **delayed partial behavioral recovery.**

144 (A) Experimental design, illustrating timeline of behavioral assays with termination points – groups
145 ended either on the 21st, or later than the 64th post-infusion day. (B) Left panel: TH-DAB staining of
146 the SN, 10x magnification and 60x magnification for vehicle and 6-OHDA-infused mouse. Scalebar left

147 200µm, scalebar right 25µm. Right panel: ratio of ipsilateral (infusion side) to contralateral side of
148 surviving TH-positive neurons in SN at 21st post-infusion day. (C) Left: spontaneous locomotion of mice
149 in open field arena for a 10 min session. Left, examples of an ACSF-infused mouse (vehicle), right
150 example of a 6-OHDA-infused mouse at baseline (upper panels), 4th post-infusion day (middle panels)
151 and 68th post-infusion day (lower panels). Right: ratio of ipsilateral to contralateral turning behavior
152 for all experimental groups plotted against session days. Note recovery in the 6-OHDA-treated mice
153 from day 4 to day 68 after initial strong turning bias (>90%). (D) Cylinder test quantified by ratio of
154 contra- to ipsilateral forepaw use. Note significant loss of contralateral forepaw involvement, both at
155 21 and 64 days. All data are presented as mean ± standard error of mean (SEM).

156

157

158 ## Surviving SN DA neurons in the early post-6-OHDA phase exhibit impaired firing properties both
159 ## *in vivo* and *in vitro*

160

161 In the early post-6-OHDA phase, we explored the *in vivo* spontaneous activity of surviving identified
162 SN DA neurons in isoflurane-anesthetized mice, using single-unit extracellular recordings combined
163 with juxtacellular labelling and post-hoc TH immunohistochemistry (see schema Fig. 2A). Figure 2B
164 shows the *in vivo* extracellular electrical activity (top panel) and identification of a representative SN
165 DA neuron (lower right panel) from a control mouse, 3 weeks after vehicle infusion. Note the typical
166 combination of irregular single spike firing with occurrence of transient fast burst discharges (bursts
167 were defined by the 80/160ms Grace criteria; see methods for details). The interspike interval (ISI)
168 histogram, which captures ISIs from the entire recording time of 10 min for this cell, displays the typical
169 features of an *in vivo* bursty DA neuron, i.e. a bimodal ISI distribution representing intra- and interburst
170 intervals over the dynamic range between ~30-1000 ms (lower left panel). This recorded and labelled
171 cell was localized in the medial SN and characterized as TH-immunopositive. In comparison, Fig. 2C

172 displays representative *in vivo* activity of a surviving identified SN DA neuron 3 weeks after 6-OHDA-
173 infusion. Here, while irregular single-spike pacemaking was present similar to controls, fast burst
174 events were almost completely absent (top panel). In accordance, the ISI histogram of this neuron, for
175 the entire 10 min of recording, showed a unimodal, Gaussian-like distribution without fast intraburst
176 and slow interburst intervals (Fig. 2C, lower left panel). This recorded and labelled cell was also
177 localized in the medial SN and identified as TH-immunopositive.

178 Similar to these two example cells, all *in vivo* recorded DA neurons from the early phase were
179 successfully juxtacellularly labeled with neurobiotin (NB), post-hoc immunohistochemically
180 reconstructed and localized within the ventral midbrain (Fig 2D, vehicle: n =28, N =15; 6-OHDA: n =18,
181 N =16). For best comparison, we restricted our analysis to those DA midbrain neurons localized in the
182 medial half of the SN (mSN), where a sufficient number of surviving and electrically active DA neurons
183 could be sampled after 6-OHDA lesion. In contrast, we only managed to detect a very small number
184 of active DA neurons in the lateral SN (lSN), the most vulnerable part of the DA midbrain (Figure 2D).
185 Consequently, Figure 2 E-H compares the group data of surviving mSN DA neurons at early phase
186 between vehicle and 6-OHDA treatment. We detected only a small reduction (< 40 %) of overall firing
187 rate for post-6-OHDA mSN DA neurons compared to vehicle-treated controls (Fig.2E; vehicle: mean
188 frequency = 7.5 ± 0.92 Hz, 6-OHDA: mean frequency = 4.71 ± 0.6 Hz, p = 0.0184, Mann-Whitney test)
189 and no differences in overall firing regularity expressed as CV (Fig. 2F; vehicle: CV = 53.96 ± 7.78 %, 6-
190 OHDA: CV = 36.06 ± 3.7 %, p = 0.1694, Mann-Whitney test). In contrast, the reduction of bursting -
191 expressed as the percentage of spikes fired in bursts (SFB) and burst rate - was dramatic (ca. 10-fold)
192 and highly significant for mSN DA neurons in the 6-OHDA group compared to vehicle controls (Fig. 2G,
193 vehicle: SFB = 31.22 ± 7.71; 6-OHDA: SFB = 2.24 ± 1.09 %; p = 0.0032, Welch's t test; Fig. 2H, vehicle:
194 burst rate = 0.34 ± 0.09 Hz, 6-OHDA: burst rate = 0.04 ± 0.02 Hz; p = 0.0066, Welch's t test). All other
195 analyzed firing parameters identified no additional differences between the two early groups (Suppl.
196 Fig. 4). In summary, we detected a dramatic compression of the dynamic *in vivo* firing range in mSN
197 DA neurons surviving the 6-OHDA lesion. In addition to the degree of DA cell loss, this functional

198 impairment of surviving DA neurons might be a novel contributing factor to the extensive motor
199 impairment, observed during the early post-6-OHDA phase.

200 Burst discharge in DA neurons is orchestrated by the interplay of patterned synaptic inputs with their
201 intrinsic excitability, giving rise to different types of bursting (Otomo et al., 2020). To identify a possible
202 contribution of cell-autonomous changes in intrinsic excitability of surviving mSN DA neurons to their
203 impaired *in vivo* bursting, we also studied these cells *in vitro* in synaptic isolation (see Schema 2I).
204 Figure 2J shows representative stable and regular pacemaker activity of identified mSN DA neuron
205 from a vehicle-infused control (lower right panel), as well as a subthreshold response to
206 hyperpolarizing current injection (lower left panel). In contrast, pacemaker activity of mSN DA neurons
207 post-6-OHDA infusion was unstable and characterized by intermittent periods of action potential
208 failure (see Fig. 2K, upper panel). However, subthreshold responses were similar to controls (lower
209 right panel). Analogous to the *in vivo* experiments, all *in vitro* recorded DA neurons were neurobiotin
210 (NB) filled, identified, and mapped, resulting in an equivalent, medial clustering of surviving SN DA
211 neurons (Fig. 2L). When *in vitro* pacemaker properties were compared between identified mSN DA
212 neurons from the vehicle and the 6-OHDA groups (Fig. 2L), we detected no differences in mean firing
213 rates (Fig. 2M, vehicle: firing rate = 1.699 ± 0.17 Hz, 6-OHDA: firing rate = 2.425± 0.25 Hz, p = 0.1448,
214 Mann-Whitney test), rebound delays and sag-amplitudes (Fig. 2O, vehicle: rebound delay = 584.9 ±
215 95.8ms, 6-OHDA: rebound delay = 429.6 ± 56.1ms, p = 0.1738, Mann-Whitney test; Fig. 2P, vehicle:
216 sag-amplitude = 15.3 ± 1.1 mV, 6-OHDA: sag-amplitude = 13.5 ± 0.96 mV, p = 0.1395, Mann-Whitney
217 test), but a highly significant 5-fold increase of pacemaker irregularity expressed as CV (Fig.2N, vehicle:
218 CV = 6.531 ± 0.7147 %; 6-OHDA: CV = 33.99 ± 5.788; p = 0.0007, Mann-Whitney test). More detailed
219 analysis revealed that the increased CV was mainly mediated by intermittent phases of firing failure,
220 similar to the one shown in Fig. 2K (Suppl. Fig. 5). Further analysis, including a comparison of on-cell
221 and whole-cell recordings, did not reveal additional differences. In short, we provided the first data
222 set in the literature that surviving SN DA neurons 3-weeks after a 6-OHDA infusion are functionally
223 impaired displaying a 10-fold reduced *in vivo* burst activity. This was accompanied by a 5-fold decrease
224 of *in vitro* cell-autonomous pacemaker stability. In order to address the question whether these

225 altered properties were stable adaptions or reflected only transient impairment, we also studied *in*

226 *vivo* and *in vitro* electrophysiology of surviving mSN DA neurons in the late phase, characterized by

227 partial behavioral recovery.

228

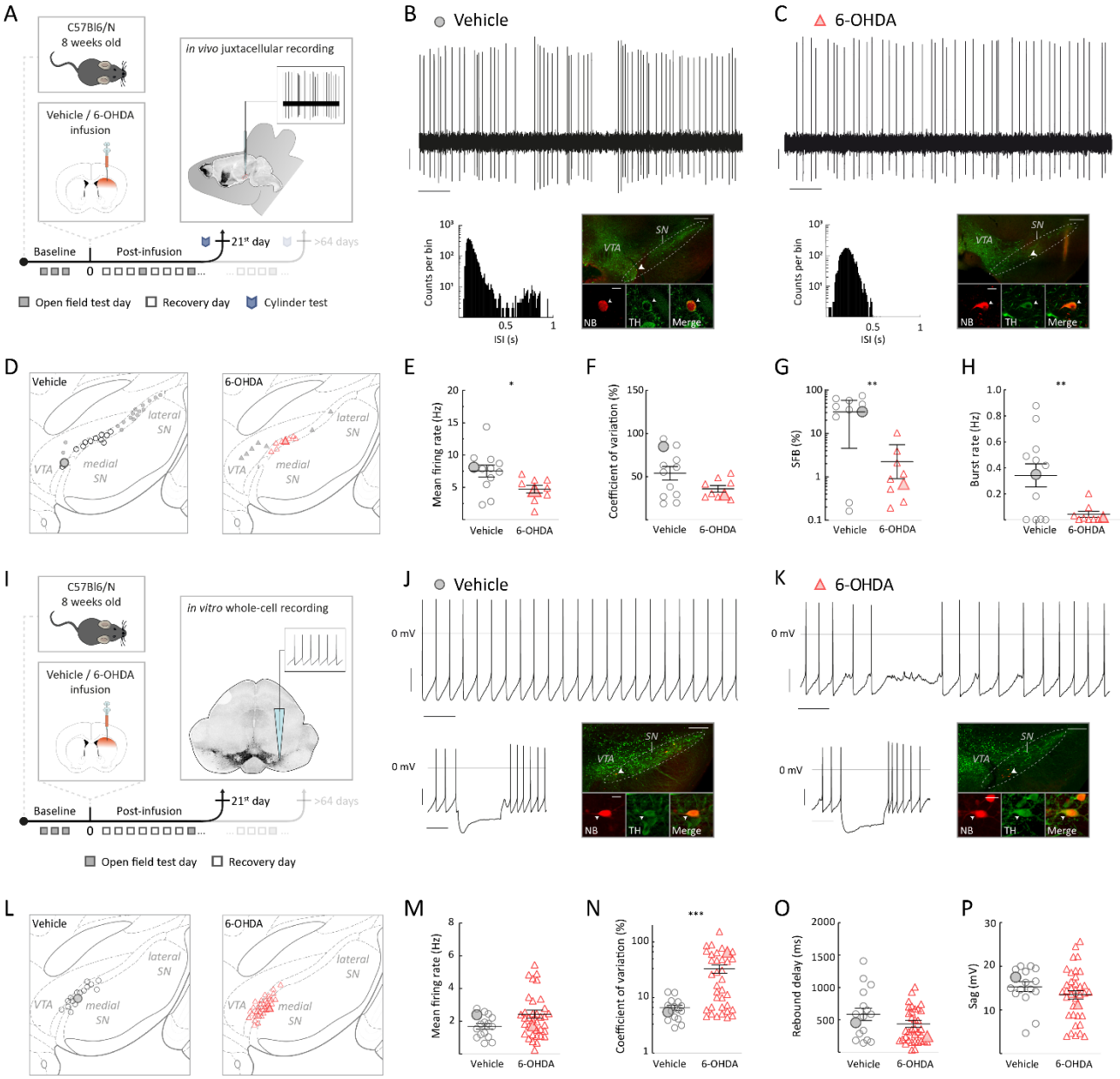

229

230 **Figure 2. Surviving SN DA neurons at early post-6-OHDA phase exhibited a 10-fold decrease in *in***

231 ***vivo* bursting and a 5-fold decree in *in vitro* regularity**

232 (A), (I) Experimental design, illustrating timeline of behavioral assays, followed by terminal *in vivo*
233 juxtacellular recordings (A) or by terminal *in vitro* whole-cell recordings (I) at the 21st post-infusion
234 day. (B), (C) Top: 10s original recording trace of spontaneous *in vivo* single-unit activity from SN DA
235 neurons in vehicle (B) and 6-OHDA-infused mouse (C). Scalebars: 1s, 0.2mV. Below, left: corresponding
236 ISI histograms. Below, right: corresponding confocal images of juxtacellularly labelled and
237 immunohistochemically identified DA neuron. Note the sparse bursting of the surviving SN DA neuron
238 from the 6-OHDA-infused mouse at early phase. (D), (L) Anatomical mapping of all extracellularly
239 recorded and juxtacellularly labelled DA neurons (D), and of all in vitro recorded and filled DA neurons
240 (L), projected to bregma -3.08 mm. Location of example SN DA neurons in (B), (C), (J), (K) are
241 highlighted. Smaller symbols represent DA neurons that have been recorded and identified, but not
242 included in the group data analysis in (E-H). (E-H) Scatter dot-plots, showing significant decrease of *in*
243 *vivo* mean firing rate (E), percentage of SFB (G) and burst rate (H) and no significant differences in CV
244 (F) between the vehicle and 6-OHDA-infused mice. Note the 10-fold decrease in SFB for 6-OHDA-
245 infused mice. (J), (K) Top: 10s original recording trace of *in vitro* whole-cell recording of spontaneous
246 SN DA neuron activity in a vehicle (J) and 6-OHDA-infused (K) mouse. Scalebars: 1s, 20mV. Note that
247 the 6-OHDA DA neuron has a highly irregular pacemaking. Below, left: corresponding to
248 hyperpolarizing current injection. Below, right: confocal images of NB filled and
249 immunohistochemically identified DA neuron. (M-P) Scatter dot-plots, showing no difference in *in*
250 *vitro* mean firing rate (M), rebound delay (O) or sag-component (P) and a 5-fold increase in CV (N).
251 Immunohistochemical imaging for all four DA neurons are displayed in 10x and 60x magnifications
252 (green, TH; red, NB), scalebars: 200µm, 20µm. All data are presented as mean ± standard error of
253 mean (SEM).

254

255

256 Surviving mSN DA neurons in the late 6-OHDA phase display full recovery of *in vivo* burst firing
257 associated with accelerated *in vitro* pacemaking
258

259 We studied and analyzed surviving mSN DA neurons in the late 6-OHDA phase in an identical fashion
260 to the early phase (compare Fig. 3A/I and Fig. 2A/I). In contrast to the 10-fold difference in burst rate
261 in early phase, we found no significant electrophysiological *in vivo* differences between the two groups
262 in the late phase (compare Fig 3B with Fig. 3C). Among others (Suppl. Fig. 6), this implies that mean
263 firing frequencies, CV, SFB and burst rates were similar in chronically surviving mSN DA neurons
264 compared to controls (Fig. 3E, vehicle: mean firing rate = 6.95 ± 0.82 Hz; 6-OHDA: mean firing rate =
265 7.53 ± 1.12 Hz; p = 0.6038, Mann-Whitney test; Fig. 3F, vehicle: CV = 54.88 ± 12.23% ; 6-OHDA: CV =
266 53.33 ± 12.65%, p > 0.9999, Mann-Whitney test; Fig. 3G, vehicle: SFB = 20.2 ± 9.11%, 6-OHDA: SFB =
267 22.17 ± 8.87%, p = 0.8784, Mann-Whitney test; Fig. 3H, vehicle: burst rate = 0.1728 ± 0.08 Hz; 6-OHDA:
268 burst rate = 0.3071 ± 0.15Hz, p = 0.4308, Mann-Whitney test). This suggests that surviving mSN DA
269 neurons might have fully recovered more than 2-months after lesion. However, the *in vivo* results
270 cannot distinguish between simple recovery (e.g. functional restoration) or adaptive homeostatic
271 plasticity. Therefore, we also studied *in vitro* pacemaker properties of the DA neurons in the late post-
272 6-OHDA phase. Here, we found clear evidence for chronic functional remodeling of surviving mSN DA
273 neurons. When comparing intrinsic pacemaker frequencies, we noticed that late 6-OHDA survivors
274 discharged almost 2-fold faster compared to vehicle-controls (compare Fig. 3J with 3K, Fig. 3M vehicle:
275 firing rate = 1.474 ± 0.1653 Hz; 6-OHDA: firing rate = 2.713 ± 0.2057 Hz, p = 0.0016, Mann-Whitney
276 test), while maintaining a stable and regular pattern (Fig. 3N, vehicle: CV = 9.515 ± 1.7 %, 6-OHDA: CV
277 = 16.10 ± 6.661 %, p = 0.175, Mann-Whitney test). In line with this pacemaker acceleration, the sag
278 component was increased, and the rebound delay shortened (Fig 3O, vehicle: rebound delay = 629.6
279 ± 96.38 ms, 6-OHDA: rebound delay = 364.2 ± 57.6 ms, p = 0.0216, Mann-Whitney test; Fig. 3P, vehicle:
280 sag-amplitude = 15.06 ± 0.9487 mV, 6-OHDA: sag-amplitude = 19.11 ± 0.9118 mV, p = 0.0072, Mann-
281 Whitney test). Other *in vitro* spike features were not significantly different between the two groups
282 (Suppl. Fig. 7). Interestingly, breaking into whole-cell recording mode further accelerated firing

frequency, while only marginally increasing firing irregularity (Suppl. Fig. 7F). In summary, complete functional recovery of surviving mSN DA neurons was – at least in part – achieved by homeostatic plasticity of intrinsic excitability. Precisely, surviving mSN DA neurons not only recovered from instable pacemaking at the early phase, but managed to double their discharge rates in late phase. As this phenotype is reminiscent to the chronic adaptation of mSN DA neurons to mutant α-synuclein overexpression, (Subramaniam et al., 2014a), we aimed to identify the underlying biophysical and molecular changes.

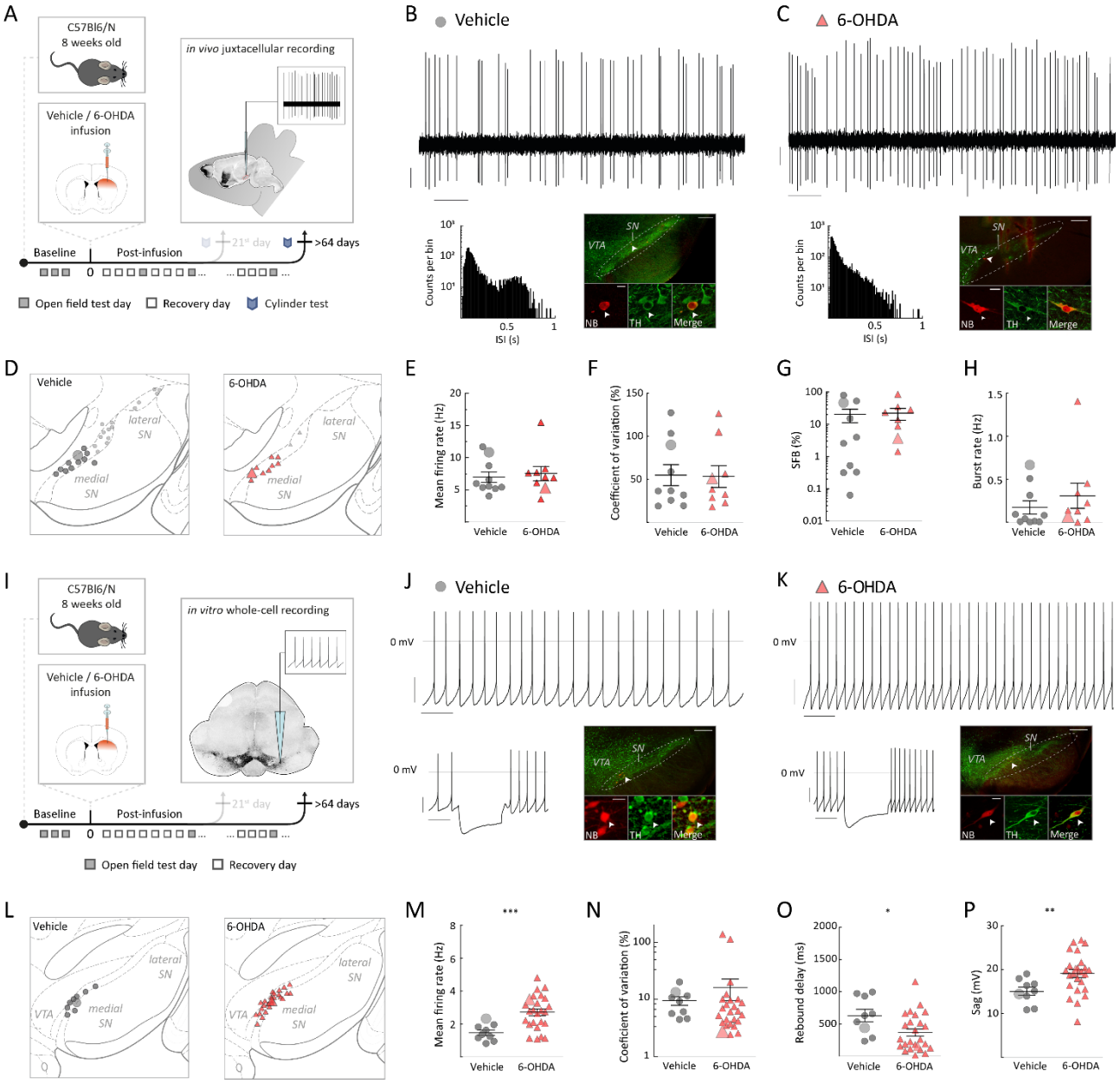

Figure 3. Surviving SN DA neurons at late 6-OHDA phase recovered *in vivo* burst firing and doubled their intrinsic pacemaker frequency *in vitro*.

293 (A), (I) Experimental design, illustrating timeline of behavioral assays, followed by terminal *in vivo*
294 juxtacellular recordings (A) or by terminal *in vitro* whole-cell recordings (I) after >64 post-infusion days.
295 (B), (C) Top: 10s original recording trace of spontaneous *in vivo* single-unit activity from SN DA neurons
296 in vehicle (B) and 6-OHDA-infused mouse (C). Scalebars: 1s, 0.2mV. Below, left: corresponding ISI
297 histograms. Below, right: corresponding confocal images of juxtacellularly labelled and
298 immunohistochemically identified DA neuron. (D), (L) Anatomical mapping of all extracellularly
299 recorded and juxtacellularly labelled DA neurons (D), and of all *in vitro* recorded and filled DA neurons
300 (L), projected to bregma -3.40 mm (D) and -3.08mm (L). Location of example SN DA neurons in (B), (C),
301 (J), (K) are highlighted. Smaller symbols represent DA neurons that have been recorded and identified,
302 but not included in the group data analysis in (E-H). (E-H) Scatter dot-plots, showing no significant
303 difference in mean firing rate (E), CV (F), SFB (G) and burst rate (H). (J), (K) Top: 10s original recording
304 trace of *in vitro* whole-cell recording of spontaneous activity from SN DA neurons in a vehicle (J) and
305 6-OHDA-infused (K) mouse. Scalebars: 1s, 20mV. Note that the 6-OHDA DA neuron has enhanced, but
306 regular pacemaking. Below, left, corresponding to hyperpolarizing current injection. Below, right,
307 confocal images of NB filled and immunohistochemically identified DA neuron. (M-P) Scatter dot-plots,
308 showing doubling of the firing rate (M), no difference in CV (N), decrease in rebound delay (O) and
309 increase of sag-component (P) for the 6-OHDA-treated mice in comparison to vehicle group.
310 Immunohistochemical imaging for all four DA neurons are displayed in 10x and 60x magnifications
311 (green, TH; red, NB), scalebars: 200µm, 20µm. All data are presented as mean ± standard error of
312 mean (SEM).

313

314

315 ## Accelerated *in vitro* pacemaking of surviving mSN DA neurons is caused by downregulation of
316 Kv4.3 channels

317

318 To test whether Kv4.3-mediated A-type channels are responsible for differences in late phase
319 pacemaker rate between 6-OHDA and controls, we carried out a pharmacological occlusion
320 experiment using 1µM AmmTx3, a selective Kv4.3 channel blocker (see scheme Fig. 4A). The presence
321 of 1µM AmmTx3 not only accelerated discharge rates in both identified mSN DA neurons from vehicle-
322 and 6-OHDA-infused mice (see Fig. 4BC for representative cells; Fig. 4D for mapping) but, importantly,
323 also eliminated significant rate differences between the two treatment groups (Fig. 4E, vehicle: mean
324 firing rate = 4.54 ± 0.18Hz, 6-OHDA: mean firing rate = 4.84 ± 0.28 Hz, p = 0.285; Fig. 4 F, vehicle: CV =
325 7.84 ± 1.26 %, 6-OHDA: CV = 5.53 ± 0.44%, p = 0.2517; both Mann-Whitney test). This result
326 demonstrated that differences in Kv4.3 channel function were a main driver of the late post-6OHDA
327 fast pacemaker phenotype. In addition, 1µM AmmTx3 also abolished more subtle differences in
328 rebound delays and sag amplitudes (Fig. 4G, vehicle: rebound delay = 31.71 ± 2.4ms, 6-OHDA: rebound
329 delay = 28.4 ± 4.0ms, p = 0.0952; Fig. 4H. vehicle: sag-amplitude = 15.61 ± 1.1mV, 6-OHDA: sag-
330 amplitude = 16.43 ± 0.95mV, p = 0.7434; both Mann-Whitney test, Suppl. Fig. 8). In summary, these
331 experiments demonstrated that reduced Kv4.3 function and/or expression are mediators of the post-
332 6-OHDA late phase phenotype of accelerated *in vitro* pacing.

333 Next, we aimed to reveal whether this adaptive phenotype was associated with altered Kv4.3 protein
334 expression. We performed Kv4.3 immunohistochemistry and confocal imaging in vehicle and 6-OHDA
335 treated mice both on the ipsilateral and contralateral infusion side (see scheme in Fig. 4I). We defined
336 DA-selective ROIs by using TH-immunopositive areas to measure the intensity of Kv4.3-immunosignals
337 exclusively within DA neurons (i.e. TH-signal based mask) (Subramaniam *et al.*, 2014a). Figure 4J and
338 4K compare Kv4.3-immunoreactivities in the midbrain between/from contralateral control side and
339 ipsilateral affected side in a 6-OHDA-treated mouse in the late post-6-OHDA phase. Note the reduction
340 of TH-immunoreactivity on the ipsilateral side (upper panels). Higher resolution of Kv4.3-
341 immunoreactivity in surviving TH-positive neurons showed lower Kv4.3-immunosignal on the treated
342 side. Quantitative comparison of TH-ROIs of the entire SN between contralateral control side and 6-
343 OHDA-treated side revealed a significant reduction of average Kv4.3-immunosignal on the 6-OHDA
344 treated side (Figure 4L, D = 0.2014, p < 0.0001, two-sample Kolmogorov–Smirnov test). This reduction

345 was also detected in a selective analysis of Kv4.3-immunosignals in the medial SN (Figure 4M,
346 contralateral side: 73.03 ± 0.389, ipsilateral side: 54.8 ± 0.486, $p < 0.0001$, unpaired t-test), the region
347 where we carried out our functional characterization. In addition, Kv4.3 signal intensities showed
348 weak correlation to the size of TH-positive ROIs ($R2 = 0.0041$, $Sy.x = 1227$, $N = 4874$, $p < 0.0001$, simple
349 linear regression, Suppl. Fig. 9). As Kv4.3 channel subunits are expected to be mostly located on the
350 cell membrane, we also investigated whether Kv4.3-immunosignal was different across cell
351 compartments. A decrease of Kv4.3-immunosignal was observed both in cell membrane and
352 cytoplasm ROIs (Suppl. Fig. 9). In contrast, analogous quantification in vehicle-treated mice revealed
353 no contra-ipsilateral differences in Kv4.3-immunoreactivity (Suppl. Fig. 9). In summary, these
354 immunohistochemical experiments provided evidence for a downregulation of Kv4.3 channel subunits
355 in mSN DA neurons, surviving a partial 6-OHDA lesion. This phenotype was therefore distinct from the
356 overexpression of Kv4.3 channel protein, observed in mutant α-synuclein mice (Subramaniam *et al.*,
357 2014a). Thus, we provided first evidence for a selective functional adaptation of SN DA neurons in
358 response to a single-hit non-progressive lesion.

359

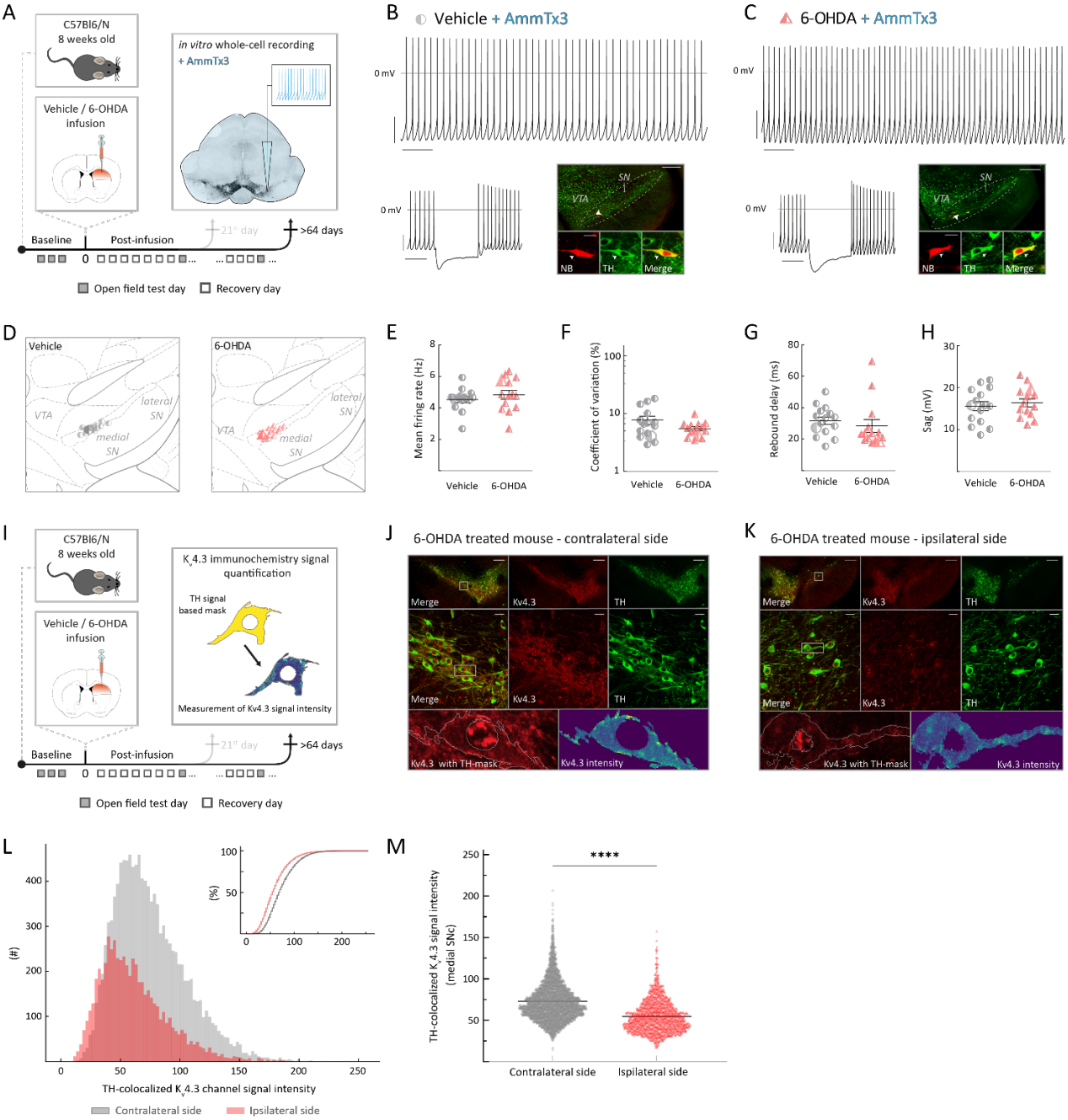

Figure 4. Enhanced pacemaker frequency of SN DA neurons at the late post-6-OHDA phase was mediated by K_v4.3 channel downregulation

(A), (I) Experimental design, illustrating timeline of behavioral assays, followed by terminal *in vitro* whole-cell recordings under K_v4.3 channel blocker AmmTx3 (A) or by multi-labeling immunohistochemistry for exploring K_v4.3-channel expression differences (I) after >64 post-infusion days. (B), (C) Top: 10s original recording traces of *in vitro* whole-cell recording of spontaneous activity from SN DA neurons in AmmTx3-preincubated slices for a vehicle (B) and 6-OHDA-infused (C) mouse.

368 Below, left: corresponding hyperpolarizing current injection. Scalebars: 1s, 20mV. Below, right:
369 confocal images of NB filled and immunohistochemically identified DA neuron (green, TH; red, NB).
370 10x , 60x magnification, scalebars: 200µm, 20µm. (D) Anatomical mapping of all *in vitro* recorded and
371 filled DA neurons, projected to bregma -2.92 mm. (E-H) Scatter dot-plots, showing loss of differences
372 in *in vitro* electrophysiological parameters. (J), (K) Top: 4x magnification of midbrain of a 6-OHDA-
373 infused mouse, >64 days post-lesion – contralateral side (J), and corresponding ipsilateral side (K).
374 Middle: 60x magnification in the highlighted area from 4x image (green, TH; red, Kv4.3). Bottom, left:
375 zoom-in on an example ROI (highlighted in 60x image). Bottom, right: color-coded K_v4.3-channel
376 immunohistochemical signal intensity in the example ROI. Note Kv4.3-channel signal decrease in
377 surviving DA neurons on the ipsilateral to the injection side. (L) Histogram showing intensity of Kv4.3
378 immunosignals for all TH-positive ROIs, from ipsilateral, lesioned, side (in red) and from contralateral
379 side (in grey). Inset, same data shown as a cumulative distribution. Note a clear right-shift to lower
380 intensities for the ipsilateral side. (M) Comparison of mean TH-colocalized K_v4.3 immunosignals from
381 medial SN from ipsilateral, lesioned, side, and contralateral, as control side. All data are presented as
382 mean ± standard error of mean (SEM).

383

384

385 ## Discussion

386

387 Our study provides the first combined *in vitro* & *in vivo* electrophysiological characterization of
388 identified DA neurons in the substantia nigra, surviving a partial 6-OHDA lesion. Studying these
389 surviving SN DA neurons at two time points, we discovered time-dependent post-6-OHDA selective
390 differences of firing properties both *in vivo* and *in vitro*. Early after lesion and coinciding with
391 prominent behavioral impairments in our model, we detected a selective and dramatic (about 10-fold)
392 reduction of *in vivo* burst firing in identified surviving SN DA neurons. This is reminiscent of an early
393 study by Hollermann & Grace (Hollerman and Grace, 1990), who reported reduced bursting in putative
394 SN DA neurons one week after partial lesion. At the early time point, we also found unstable *in vitro*
395 pacemaker activity in these cells, while the mean firing rates were not different compared to those
396 from vehicle-infused controls. In contrast, late (>2 months) after lesion, where substantial behavioral
397 recovery had occurred, we detected no differences in *in vivo* firing rates and patterns – including burst
398 discharges – of surviving SN DA neurons between 6-OHDA- and vehicle-infused mice. Surprisingly, the
399 *in vitro* pacemaker rate was almost twice as fast in post-6-OHDA DA survivors compared to controls.
400 Finally, we identified Kv4.3 channel downregulation as the cause for this chronic post-lesional
401 pacemaker acceleration. In essence, we revealed for the first time the homeostatic adaptations of
402 electrophysiological properties in surviving SN DA neurons.

403 Regarding the functional phenotype of surviving SN DA neurons, we identified a sequence of early but
404 transient impairment, followed by chronic functional adaptation. While we did not investigate the
405 mechanisms underlying the early impairment of *in vivo* burst firing, we focused our in-depth analysis
406 on the chronic phase. Here, we identified a slowly-developing chronic Kv4.3 channel-mediated
407 mechanism of pacemaker adaptation. Previously, we had already identified Kv4.3 channels in SN DA
408 neurons as a pathophysiological target in a transgenic mutant (A53T-SNCA) α-synuclein mouse model
409 (without cell loss) (Subramaniam *et al.*, 2014a). In this model, we found a pacemaker acceleration
410 caused by oxidative impairment of Kv4.3 channels. In contrast to the post-lesional SN DA neurons in

411 this study, the activity of SN DA neurons in the α-synuclein model was accelerated also *in vivo.* Thus,
412 α-synuclein pathology causes an allostatic shift of the *in vivo* firing rate setpoint of SN DA neurons,
413 while post-lesional SN DA neurons recover their *in vivo* firing setpoint by homeostatic pacemaker
414 plasticity. Interestingly, both models converge on the pacemaker potassium channel Kv4.3 but in a
415 different fashion. While Kv4.3 subunits were downregulated on protein level in post-lesional SN DA
416 neurons, mutant α-synuclein induced oxidative Kv4.3 dysfunction as well as protein upregulation
417 (Subramaniam *et al.*, 2014a). We are aware that neither of the mouse models fully capture the
418 pathophysiology of PD, where α-synuclein pathology, cell loss, inflammation and compensatory
419 mechanisms are expected to occur side by side (Surmeier et al., 2017b). At least at the transcriptional
420 level, we know that Kv4.3 mRNA is upregulated in human SN DA neurons from PD patients (Dragicevic
421 *et al.*, 2015; Schiemann *et al.*, 2012). This is similar to α-synuclein models and opposite to post-lesional
422 Kv4.3 downregulation, shown here, suggesting that Kv4.3 channel mediated compensatory
423 mechanisms are finally overwhelmed during PD progression. Moreover, the results of this study imply
424 that α-synuclein pathology interferes with the homeostatic capacity of surviving SN DA neurons, in
425 particular the regulation of Kv4.3 channels. Indeed, we recently showed a Kv4.3 gain-of-function
426 phenotype for vagal motoneurons in response to mutant SNCA expression (Chiu et al., 2021). Thus,
427 Kv4.3 channels – a major "brake" of the pacemaker rate (Khaliq and Bean, 2008; Liss et al., 2001; Tarfa
428 et al., 2017) – is an emerging downstream target across several PD models. It would be interesting to
429 further investigate functional and molecular regulation of this potassium channel in chronic and
430 progressive PD models, where pathology and cell loss go hand in hand.

431 In addition to cell-autonomous adaptions in surviving SN DA neurons, we assume that their chronic *in*
432 *vivo* electrophysiological phenotype is also shaped by network level plasticity in response to
433 dopamine-depletion. Our finding that the mean *in vivo* discharge rates were not different to controls
434 in the presence of an accelerated intrinsic pacemaker strongly suggests a shift of the synaptic
435 excitation-inhibition (E-I) balance towards more inhibition. Numerous studies have found altered
436 synaptic inhibition in the dopamine-depleted basal ganglia (recently reviewed in (Zhang et al., 2021)).
437 In particular, Heo and colleagues recently demonstrated a chronic E-I balance shift toward more

438 inhibition across several PD models including 6-OHDA (Heo et al., 2020). They identified a substantial
439 contribution of additional GABA synthesis and release from reactive astrocytes in the midbrain. It has
440 also been well-established that basal ganglia GABA neurons fire in more synchronized hence more
441 effective fashion after dopamine depletion (Cagnan et al., 2015; Evans et al., 2020; Milosevic et al.,
442 2018; Phillips et al., 2020; Tinkhauser et al., 2020; Wichmann et al., 2018). This has recently been
443 confirmed by elegant *in vivo* single cell resolved studies using either gCAMP-based calcium monitoring
444 or *in vivo* patch-clamp approaches (Ketzef et al., 2017; Kravitz *et al.*, 2010; Parker *et al.*, 2018; Parker
445 *et al.*, 2016; Sitzia *et al.*, 2020). The chronic acceleration of pacemaker rate in response to enhanced
446 inhibition would also be expected within the framework of homeostatic plasticity (Turrigiano, 2012).
447 However, the mechanisms of firing rate set-point control, recently elucidated for hippocampal
448 neurons (Styr et al., 2019), is still unknown for SN DA neurons.

449 Our study has several limitations. As already discussed, we explored a single-hit partial lesion model,
450 while PD is a chronic progressive neurodegenerative process. While we demonstrate that
451 electrophysiological phenotypes per se are flexible and change in response to lesion, we also have to
452 consider distinct DA subpopulations within the SN. We recently showed that lateral SN DA neurons
453 projecting to DLS, the most vulnerable DA subpopulation (corresponding to the ventro-lateral SN DA
454 neurons in humans (Duzel et al., 2009; McCutcheon et al., 2019)) possess a distinct *in vivo* firing
455 phenotype in control mice (Farassat et al., 2019). Therefore, recording from this population in PD
456 models would be highly relevant. However, in our current partial 6-OHDA lesion model, these lateral
457 SN DA neurons were too severely lost to allow for more than anecdotal post-lesion
458 electrophysiological analysis (see Fig. 3). Here, a milder version of the current model would be needed
459 to identify their homeostatic plasticity. Regarding the surviving DA neuron in the medial SN, we
460 previously showed that they have distinct projection targets including DLS, DMS and lateral shell of
461 nucleus accumbens (Farassat *et al.*, 2019). In the current study, we have not aimed for identification
462 of axonal projections to avoid potentially confounding effects of additional brain surgery and to not
463 further complicate already challenging experiments. Nevertheless, this important issue should be

464 addressed in follow-up studies by e.g. molecular subtyping approaches (Heymann et al., 2020; Poulin
465 et al., 2018; Poulin et al., 2020; Saunders et al., 2018).

466 Finally, we would like to speculate about the possible implications of our findings for PD. In principle,
467 homeostatic responses, as identified here, could have a dual nature. On one hand, they might render
468 the neuron more robust, thereby slowing the rate of cell loss. On the other hand, the homeostatic
469 adaptations may amplify innate vulnerability and accelerate disease progression. The latter would be
470 a variant of the "stressful pacemaker" hypothesis of DA vulnerability (Chan et al., 2007; Surmeier,
471 2007; Surmeier et al., 2017a) and its potential clinical implications (Guzman et al., 2018; Liss and
472 Striessnig, 2019; Ortner, 2021; Ortner et al., 2017; Parkinson Study Group, 2020). In summary, we
473 provide the first steps towards defining the homeostatic repertoire of surviving DA neurons, but
474 deeper insights are necessary to rationally design neuroprotective interventions in PD.

475

476 # Methods

477 ## Animals

478 Male C57Bl6/N mice (Charles River Laboratories) were used for the study. Mice were 8 weeks old,
479 group housed and maintained on a 12-hour light-dark cycle. All experiments and procedures involving
480 mice were approved by the German Regierungspräsidium Darmstadt (V54-19c20/15-F40/30). In total,
481 115 mice were used for this study (see table below).

	Early phase		**Late phase**	
	Mice (#)	Cells (#)	Mice (#)	Cells (#)
***In vivo* juxta & behavior – vehicle**	15	12 – medial/ 28 – all	12	10 – medial/ 26 – all
***In vivo* juxta & behavior – 6-OHDA**	16	9 – medial/ 16 – all	10	9 – medial/ 11 – all
***In vitro* – vehicle**	3	16	2	9
***In vitro* – 6-OHDA**	6	37	5	25
***In vitro* & AmmTx3 – vehicle**	-	-	3	15
***In vitro* & AmmTx3 – 6-OHDA**	-	-	3	14
	Mice (#)		Mice (#)	
Kv4.3 Immunochemistry	8		8	
SN quantification – vehicle	9		3	
SN quantification – 6-OHDA	9		3	
Sum = 115				

482

483 ## Stereotactic 6-OHDA infusion

484 All surgeries were performed under general anesthesia in areflexic state. Prior to the induction of
485 anesthesia, a premedication of 0.2 mg/kg atropine (atropine-sulfate, Braun Melsungen AG,
486 Melsungen) was given as an intraperitoneal (i.p.) injection to stabilize circulation. Anesthesia was
487 induced in a plastic chamber, which was flooded with 5% Isoflurane (Florene®, AbbVie Deutschland
488 GmbH & Co. KG, Ludwigshafen, Germany) in pure oxygen (0.4 l/min). For maintenance of anesthesia,
489 isoflurane was delivered through a breathing mask with a flow rate of 0.35 l/min and its concentration
490 was regulated to 1.5-2.2% using an adjustable vaporizer (Uno, Zevenaar, Netherlands). The depth of
491 anesthesia was controlled by testing the toe pinch reflex and the breathing rate (1-2Hz). Body
492 temperature (36°C) and respiration were constantly monitored. Lidocaine/prilocaine ointment (25

493 mg/g, Emla® creme, AstraZeneca GmbH, 22876 Wedel) was applied prior to surgery and after suturing
494 of the wound as local anesthetics. Additional analgesia was provided by subcutaneous injection of
495 carprofen (4 mg/kg in NaCl, 1:100, Rimadyl®, Pfilzer GmbH, Berlin, Germany) after infusion. Eye
496 lubricant (Visidic, Bausch and Lomb, Berlin, Germany) was used to protect eyes from desiccation.

497 Desipramine hydrochloride (20 mg/kg, Sigma Aldrich) was injected i.p. 20-40 min before intracranial
498 infusions to prevent 6-OHDA uptake by noradrenergic neurons. The desipramine solution was
499 prepared in sterile, isotonic NaCl solution (B. Braun Melsungen AG, Germany) at the day of surgery.
500 The infusion solutions are based on sterile artificial cerebrospinal fluid (ACSF, Harvard Apparatus,
501 Holliston, MA, USA) with 0.2% L-ascorbic acid (used also as a vehicle solution). The 6-OHDA solution
502 (0.02% 6-hydroxydopamine hydrochloride in ACSF with 0.2% L-ascorbic acid) was prepared at the day
503 of infusion, stored on ice, and shielded from light.

504 During surgery, the animals were placed on a heating pad and were fixed in a stereotactic frame
505 (Model 1900, Kopf Instruments, Tujunga, USA) with a stereotactic arm and a connected three-way
506 digital positioning display. The scalp was opened by a longitudinal cut to expose the skull with bregma
507 and lambda on display. With a centering scope (Model 1915, Kopf Instruments, Tujunga, USA), the
508 bregma-lambda distance was measured and examined for suitable anatomy (4.4±0.2 mm distance).
509 Afterwards, the skull was aligned to a reference frame with a stereotaxic alignment indicator (Model
510 1905, Kopf Instruments, Tujunga, USA) and the manipulator system was referenced to bregma.

511 Using a stereotaxic drill (Model 1911, Kopf Instruments, Tujunga, USA) with a 500 µm diameter drill
512 bit, a hole above the right striatum was drilled (coordinates: ML: +1.9 mm, AP: +0.5 mm to bregma).
513 ACSF or 6-OHDA solution were loaded to a 10 µl NanoFil syringe (World Precision Instruments Inc.,
514 Sarasota, FL, USA) with a 35G blunt needle, which was mounted on a MicroSyringe Pump (UMP3-1,
515 World Precision Instruments) and controlled by a SYSMicro4 Controller (World Precision Instruments).
516 Using the stereotactic arm, the needle was slowly lowered (about 750 µm/min) to a position of -2.2
517 mm below the brain surface (infusion site coordinates: ML: +1.9 mm, AP: +0.5 mm, DV: -2.2 mm to

518 bregma). Anatomical references are based on Franklin and Paxinos (2008). A volume of 6 µl was
519 infused with a flow rate of 250 nl/min. Once the volume was infused, the needle rested for 5 minutes
520 in that position before it was slowly moved out of the brain. Directly before and after infusion, proper
521 functioning of the syringe system and the needle was checked. Finally, after suture the animal was
522 placed on a heating pad for full recovery. Oats, wet food pallets and water were placed inside the cage
523 to ease consumption.

524

525 ## Behavioral testing

526 ### *Open field*

527 Spontaneous locomotion (track length, wall distance, time in center and number of rearings) and
528 rotations of all mice were monitored in open field (50 × 50 cm, center 30 × 30 cm; red illumination, 3
529 lx) for 10 min in 3 baseline sessions and every 4th or 7th day post-infusion of ACSF/6-OHDA till the day
530 of *in vivo* or *in vitro* experiment (e.g. 21st or >68th post-operative day). The open field was cleaned
531 before and after each mouse with 0,1% acetic acid in distilled water. Using a video tracking system
532 (Viewer II/III, Biobserve) spontaneous behavior was recorded and analyzed both online and offline.
533 Data was extracted from Viewer as Excel-tables and the final analysis was made with custom made
534 Matlab-scripts.

535

536 ### *Cylinder test*

537 Forelimb use during explorative activity was explored with cylinder test. The test was performed at
538 corresponding termination time point (20-21st and 64th post-infusion day). Mice were placed
539 individually in a glass beaker (9 cm diameter, 19 cm height) at room light and were video recorded
540 with a camera (Logitech HD Webcam C615) for about 5 min. No habituation was allowed before video
541 recording. The glass cylinder was cleaned before and after every mouse with 0,1% acetic acid in
542 distilled water. Only weight-bearing wall contacts made by each and both forelimb on the cylinder

543 wall were scored. Wall exploration was expressed in terms of the percentage of contralateral to the
544 infusion side (in the 6-OHDA-infused mice also impaired forepaw) to all forelimb wall contacts.

545

546 *In vivo* electrophysiology

547 *Extracellular recording*

548 *In vivo* extracellular single-unit activities of SN and VTA neurons were recorded in ACSF-infused
549 (vehicle) and 6-OHDA-infused mice, similar procedures were used in other studies from our lab
550 (Farassat *et al.*, 2019; Schiemann *et al.*, 2012; Subramaniam *et al.*, 2014a). Briefly, mice were
551 anesthetized (isoflurane; induction 4.5-5%, maintenance 1–2% in 0.4 l/min O2) and placed into a
552 stereotactic frame. The craniotomies were performed as described above to target the lateral SN (AP:
553 -3.08 mm, ML: 1.4 mm) and medial SN (AP: -3.08 mm, ML: 0.9 mm). Borosilicate glass electrodes (10–
554 25 MΩ; Harvard Apparatus, Holliston, MA, USA) were made using a horizontal puller (DMZ-Universal
555 Puller, Zeitz, Germany) and filled with 0.5 M NaCl, 10 mM HEPES (pH 7.4) and 1.5% neurobiotin (Vector
556 Laboratories, Burlingame, CA, USA). A micromanipulator (SM-6; Luigs & Neumann, Ratingen,
557 Germany) was used to lower the electrodes to the recording site. The single-unit activity of each
558 neuron was recorded for at least 10 minutes at a sampling rate of 12.5 kHz (for firing pattern analyses),
559 and then for another one minute at a sampling rate of 20 kHz (for the fine analysis of AP waveforms).
560 Signals were amplified 1000x (ELC-03M; NPI electronics, Tamm, Germany), notch- and bandpass-
561 filtered 0.3–5000 Hz (single-pole, 6 dB/octave, DPA-2FS, NPI electronics) and recorded on a computer
562 with an EPC-10 A/D converter (Heka, Lambrecht, Germany). Simultaneously, the signals were
563 displayed on an analog oscilloscope and an audio monitor (HAMEG Instruments CombiScope HM1508;
564 AUDIS-03/12M NPI electronics). Midbrain DA neurons were initially identified by their broad biphasic
565 AP (> 1.2 ms duration) and slow frequency (1–8 Hz) (Grace and Bunney, 1984a; b; Ungless and Grace,
566 2012). AP duration was determined as the interval between the start of initial upward component and
567 the minimum of following downward component.

568

569 *Juxtacellular labeling of single neurons*

570 In order to identify the anatomical location and neurochemical identity of the recorded neurons, they
571 were labeled post-recording with neurobiotin using the juxtacellular *in vivo* labeling technique
572 (Pinault, 1996). Microiontophoretic currents were applied (1–10 nA positive current, 200ms on/off
573 pulse, ELC-03M, NPI Electronics) via the recording electrode in parallel to the monitoring of single-unit
574 activity. Labeling was considered successful, when: the firing pattern of the neuron was modulated
575 during current injection (i.e., increased activity during on-pulse and absence of activity in the off-
576 pulse), the process was stable for at least 20s, and was followed by the recovery of spontaneous
577 activity. This procedure allowed for the exact mapping of the recorded DA neuron within the SN and
578 VTA subnuclei (Franklin and Paxinos, 2008) using custom written scripts in Matlab (MathWorks,
579 Natick, MA, USA), combined with neurochemical identification using TH-immunostaining.

580

581 ## *In vitro* electrophysiology

582 *Slice preparation*

583 Animals were anesthetized by intraperitoneal injection of ketamine (250 mg/kg, Ketaset, Zoetis) and
584 medetomidine-hydrochloride (2.5 mg/kg, Domitor, OrionPharma) prior to intracardial perfusion using
585 ice-cold ACSF consisting of the following (in mM): 50 sucrose, 125 NaCl, 2.5 KCl, 25 NaHCO3, 1.25
586 NaH2PO4, 2.5 glucose, 6 MgCl2, 0.1 CaCl2 and 2.96 kynurenic acid (Sigma-Aldrich), oxygenated with
587 95% O2 and 5% CO2. Rostral coronal midbrain slices (bregma: -2.92 mm to -3.16 mm) were sectioned
588 at 250 µm using a vibrating blade microtome (VT1200s, Leica). Slices were incubated for 1 h before
589 recordings in a 37°C bath with oxygenated extracellular solution with extra 1µM AmmTx3, containing
590 the following (in mM): 22.5 sucrose, 125 NaCl, 3.5 KCl, 25 NaHCO3, 1.25 NaH2PO4, 2.5 glucose, 1.2
591 MgCl2 and 1.2 CaCl2.

592

593 *In vitro patch-clamp recordings*

594 Slices were placed in a heated recording chamber (37°C) that was perfused with oxygenated
595 extracellular solution at 2-4 ml min^{-1}. CNQX (20 µM; Biotrend), gabazine (SR95531, 4 µM; Biotrend)
596 and DL-AP5 (10 µM; Cayman Chemical) were added to inhibit excitatory and inhibitory synaptic
597 transmission. Neurons were visualized using infrared differential interference contrast
598 videomicroscopy with a digital camera (VX55, Till Photonics) connected to an upright microscope
599 (Axioskop 2, FSplus, Zeiss). Patch pipettes were pulled from borosilicate glass (GC150TF-10; Harvard
600 Apparatus LTD) using a temperature-controlled, horizontal pipette puller (DMZ-Universal Puller,
601 Zeitz). Patch pipettes (4-6 MΩ) were filled with a solution containing the following (in mM): 135 KGlu,
602 5 KCl, 10 HEPES, 0.1 EGTA, 5 MgCl2, 0.075 CaCl2, 5 NaATP, 1 LiGTP, 0.1% neurobiotin, adjusted to a
603 pH of 7.35 with KOH. Recordings were performed using an EPC-10 patch-clamp amplifier (Heka
604 electronics) with a sampling rate of 20 kHz and a low-pass filter (Bessel, 5 kHz). For analysis, action
605 potential thresholds (mV) were determined at $dV_m/dt > 10$ mV/ms.

606

607 ## Immunohistochemistry

608 Following *in vivo* recordings, animals were transcardially perfused, as described previously (Farassat
609 *et al.*, 2019; Schiemann *et al.*, 2012; Subramaniam *et al.*, 2014a). Fixed brains were sectioned into
610 60µm (midbrain) or 100µm (forebrain) coronal sections using a vibrating microtome (VT1000S, Leica).
611 *In vitro* slices were fixed in paraformaldehyde after finishing the experiment. Sections were rinsed in
612 PBS and then incubated (in blocking solution (0.2 M PBS with 10% horse serum, 0.5% Triton X-100,
613 0.2% BSA). Afterwards, sections were incubated in carrier solution (room temperature, overnight)
614 with the following primary antibodies: polyclonal guinea pig anti-tyrosine hydroxylase (TH; 1:1000;
615 Synaptic Systems), monoclonal mouse anti-TH (1:1000; Synaptic Systems) or polyclonal rabbit anti-TH
616 (1:1000; Synaptic Systems); mouse anti-Kv4.3 (1:1000, Alomone Labs). In sequence, sections were
617 again washed in PBS and incubated (room temperature, overnight) with the following secondary
618 antibodies: goat anti-guinea pig 488, goat anti-rabbit 488, goat anti-mouse 488, goat anti-mouse 568

619 (all 1:750; Thermofisher). Streptavidin AlexaFluor-568 and Streptavidin AlexaFluor-488 (both 1:1000;
620 Invitrogen) were used for identifying neurobiotin-filled cells. Sections were then rinsed in PBS and
621 mounted on slides with fluorescent mounting medium (Vectashield, Vector Laboratories).

622

623 ## DAB immunocytochemistry

624 For DAB (3,3'-diaminobenzidine) staining procedures, a Vectastain ABC Staining Kit (Vector
625 Laboratories) was used. Coronal sections of midbrain (30 µm) areas were cut and rinsed in PBS (3x10
626 min). Similar to previous immunolabeling procedures, unspecific antigen binding sites were blocked
627 by incubation of the sections with blocking solution (60 min, room temperature). Subsequently,
628 sections were incubated with primary antibody against TH (rabbit anti TH) overnight, rinsed in PBS
629 (3x10 min), and were incubated with biotinylated secondary antibodies (biotinylated anti-rabbit) for
630 two hours at RT. In parallel, an avidin-biotin complex (ABC) was formed by pre-incubation of avidin
631 (1:1000) with biotinylated HRP (1:1000) in PBS for two hours at room temperature. Sections were
632 rinsed in PBS (3x10 min) prior to incubation with ABC solution (60 min, room temperature). Next,
633 sections were rinsed in PBS (2x10 min) and Tris-buffer (1x10 min). Finally, DAB oxidation was
634 developed by application of 2 % H_2O_2, 2 % $NiCl_2$ and 4 % DAB in Tris-buffer using a DAB Substrate Kit
635 (Vector Laboratories, Burlingame, USA). $NiCl_2$ enhances sensitivity and intensity of DAB precipitation
636 product. DAB oxidation was developed for 2 to 5 minutes and was stopped with Tris-buffer once a
637 specific high-contrast signal was detectable. Sections were rinsed in Tris-buffer (3x10 min) and
638 transferred onto gelatin-covered slides, air-dried overnight, and dehydrated in consecutive ascending
639 alcohol concentrations (50 %, 70 %, 90 % and 2x 100 %; 10 min each) followed by dehydration in xylol
640 (2x 100 %; 10 min each). Finally, sections were mounted under glass coverslips with hardening
641 mounting medium (Vectamount, Vector Laboratories, Burlingame, USA).

642

643 ## Unbiased stereology measurements

644 For quantification of total cell loss, TH-DAB labeled SN DA neurons were counted using unbiased
645 stereology based on optical dissection (Gundersen, 1986). In coronal sections (30 µm), the region of
646 interest was selected based on anatomical landmarks including the medial lemniscus, which separates
647 SN and adjacent VTA. Stereological counting provides unbiased data based on random, systematic
648 sampling using an optical fractionator. This method involves counting of neurons with an optical
649 dissector, a three-dimensional probe placed through a reference space (Gundersen, 1986). The optical
650 dissector forms a focal plane with a thin depth of field through the selected sections. Objects in focus
651 of this focal plane are located within the reference section and are counted, while objects outside of
652 the focal plane are not counted. On top of the optical dissector, a counting frame is applied. Counting
653 frames ensure that all neurons have equal probabilities of being selected, regardless of shape, size,
654 orientation, and distribution. To avoid counting of capped neurons at the border of a section, an
655 additional guard zone was deployed at the upper and lower borders of each section. DA neurons
656 within the counting frame as well as those crossing the green line (acceptance line) were counted,
657 while DA neurons crossing the red line (rejection line) excluded. Moreover, only neurons with a
658 detectable nucleus in focus within the optical dissector were counted. For quantification of total cell
659 loss, StereoInvestigator software (V5, MicroBrightField, Colchester, USA) was used in combination
660 with BX61 microscope (Olympus, Hamburg, Germany). The region of interest was selected and marked
661 using a low magnification objective lens (2x, NA 0.25, Olympus) and 12-30 serial sections of 30 µm
662 thickness were counted, covering the entire caudo-rostral extent of the SN. To count the number of
663 DA neurons in the area of the SN pars compacta, a high magnification oil-immersion objective lens
664 (100x, NA 1.30, Olympus) was used.

665

666 ## Optical density measurements

667 Optical density measurements of TH-DAB labeled striatal sections were performed using ImageJ
668 software (http://rsbweb.nih.gov/ij/). Following TH-DAB labeling and TH-immunohistochemistry,

669 images of five coronal sections (100 µm) covering the rostrocaudal axis of the striatum were captured
670 using laser-scanning microscope (Nikon Eclipse90i, Nikon GmbH). Images were gray scale converted
671 and mean gray values of desired striatal areas were encircled and measured. Unspecific mean gray
672 values were measured in a defined cortical area (100x100 pixels) that displayed no specific TH signal
673 due to the absence of DA innervation and were subtracted. The ventral edge of lateral ventricles
674 served as an anatomical landmark to separate dorsal and ventral areas. For all animals, the
675 measurement from the ipsilateral to the infusion side were divided by the contralateral side to
676 calculate the relative optical density of the striatum.

677

678 ## Immunohistochemical Kv4.3 channel signal quantification

679 A Nikon Eclipse 90i microscope was used for fluorescent signal detection, excitation wavelength of
680 488 nm for TH-signal and 568 nm for Kv4.3-channel signal. From each animal, 4 midbrain slices
681 covering the caudal, intermedial and rostral regions, were selected and imaged for overview with 4x
682 magnification. Then 60x magnification was used to acquire data from 4 areas within each SN (4 images
683 on the ipsilateral and 4 images on the contralateral to infusion side). All images were acquired using
684 the same laser and camera settings. Images were exported from Nikon NIS-Elements Advanced
685 Research (Version 4.20.03) software as 8-bit TIFF files for quantification. Data was analyzed using
686 custom made Python 3.0 scripts with matplotlib, numpy, scimage and scipy modules. First, TH
687 immunosignals were converted to a binary image via Otsu-thresholding algorithm. Then, the resulting
688 binary image was used as a mask for Kv4.3 channel immunosignal detection. For all ROIs surface areas
689 and mean Kv.4.3 channel signal intensity was measured. By applying erosion and dilatation algorithms
690 on the ROIs, membrane and cytoplasm areas were segregated, allowing isolation of Kv4.3 channel
691 immunosignal intensity for these cell compartments. Background Kv4.3 channel immunosignal was
692 quantified in TH-immunosignal areas below the Otsu-threshold. All data were then grouped according
693 to medio-lateral and ipsi-/contralateral position for both vehicle and 6-OHDA group. Graphs and
694 statistical analysis for this data was performed using Python custom made scripts.

695

696 ## Statistical Analysis

697 ### *Spike train analyses*

698 Spike time-stamps were extracted by thresholding above noise levels with IgorPro 6.02 (WaveMetrics,
699 Lake Oswego, OR, USA). Firing pattern properties such as mean frequency, coefficient of variation (CV)
700 and bursting measures were analyzed using custom scripts in Matlab. In order to estimate burstiness
701 and intra-burst properties, we used the burst detection methods described in Grace & Bunney (Grace
702 and Bunney, 1984a; b). All non-burst related ISIs (excluding all ISIs that followed the Grace and Bunney
703 criteria, as well as all pre- and post-burst ISIs) were used to calculate the single spike firing frequency
704 and single spike coefficient of variation.

705 For analysis of general firing patterns, autocorrelation histograms (ACH) were plotted using custom
706 Matlab scripts. We used established criteria for classification of *in vivo* firing patterns based on visual
707 inspection of autocorrelograms (Farassat *et al.*, 2019; Schiemann *et al.*, 2012; Subramaniam *et al.*,
708 2014a): single spike-oscillatory (≥3 equidistant peaks with decreasing amplitudes), single spike-
709 irregular (<3 peaks, increasing from zero approximating a steady state), bursty-irregular (narrow peak
710 with steep increase at short ISIs) and bursty-oscillatory (narrow peak reflecting fast intraburst ISIs
711 followed by clear trough and repetitive broader peaks).

712 ## Statistics

713 Categorical data is represented as stacked bar graphs. To investigate the assumption of normal
714 distribution, we performed the single-sample Kolmogorov-Smirnov test. The Mann-Whitney-Test,
715 one-/two-way ANOVA were performed in non-parametric data to determine statistical significance.
716 Categorical parameters, such as ACH-based firing pattern, were analyzed with the Chi-squared test.
717 Statistical significance level was set to $p < 0.05$. All data values are presented as means ± SEM.
718 Statistical tests were performed using GraphPad Prism 9 (GraphPad Software, San Diego, CA, USA),
719 Matlab and Python. The scatter plots are represented with median or mean ± SEM. The resulting *p*

720 values were compared with Bonferroni-corrected α-level or Tukey *post hoc* comparison. A value of p
721 ≤ 0.05 was considered to be statistically significant; $p \leq 0.05$ = *$p \leq 0.005$ = **$p \leq 0.0005$ = ***. Graphs
722 were plotted using GraphPad Prism software (9.0c), Matlab and Python.

723 Acknowledgements

724 This study was supported by research grants to JR (DFG CRC 1080 and CRC 1451). LK is a MD/PhD
725 candidate at TransMed, Gutenberg University Mainz. We thank Beatrice Fischer and Jasmine Sonntag
726 for technical assistance, Alexander Prinz for preliminary data on post-6-OHDA stereology and Kauê
727 Machado Costa for support in Matlab based analysis and mentoring to LK.

728 Additional information

729 Author contributions

730 LK & JR designed the study. LK performed the lesions, behavioral & *in vivo* electrophysiology, JS
731 performed the *in vitro* experiments. Analysis was carried out jointly by LK, JS, NF and JR. NF taught LK
732 *in vivo* electrophysiology and juxtacellular labelling. LK & JR wrote the manuscript.

733 Declaration of Interests

734 The authors declare no conflict of interests.

735 Author ORCIDs

736 Jochen Roeper https://orcid.org/0000-0003-2145-8742

737 Lora Kovacheva https://orcid.org/0000-0001-6999-1533

738 Josef Shin https://orcid.org/0000-0002-3556-125X

739 Ethics

740 Animal experimentation: All experiments and procedures involving mice were approved by the
741 German Regierungspräsidium Darmstadt (V54-19c20/15-F40/30).

742 ## References

743 Bez, F., Francardo, V., and Cenci, M.A. (2016). Dramatic differences in susceptibility to l-DOPA-induced
744 dyskinesia between mice that are aged before or after a nigrostriatal dopamine lesion. Neurobiol Dis
745 *94*, 213-225. 10.1016/j.nbd.2016.06.005.
746 Cagnan, H., Duff, E.P., and Brown, P. (2015). The relative phases of basal ganglia activities dynamically
747 shape effective connectivity in Parkinson's disease. Brain *138*, 1667-1678. 10.1093/brain/awv093.
748 Cenci, M.A., and Bjorklund, A. (2020). Animal models for preclinical Parkinson's research: An update
749 and critical appraisal. Prog Brain Res *252*, 27-59. 10.1016/bs.pbr.2020.02.003.
750 Chan, C.S., Guzman, J.N., Ilijic, E., Mercer, J.N., Rick, C., Tkatch, T., Meredith, G.E., and Surmeier, D.J.
751 (2007). 'Rejuvenation' protects neurons in mouse models of Parkinson's disease. Nature *447*, 1081-
752 1086. 10.1038/nature05865.
753 Chen, L., Daniels, S., Kim, Y., and Chu, H.Y. (2021). Cell Type-Specific Decrease of the Intrinsic
754 Excitability of Motor Cortical Pyramidal Neurons in Parkinsonism. J Neurosci *41*, 5553-5565.
755 10.1523/JNEUROSCI.2694-20.2021.
756 Chiu, W.H., Kovacheva, L., Musgrove, R.E., Arien-Zakay, H., Koprich, J.B., Brotchie, J.M., Yaka, R., Ben-
757 Zvi, D., Hanani, M., Roeper, J., and Goldberg, J.A. (2021). α-Synuclein-induced Kv4 channelopathy in
758 mouse vagal motoneurons drives nonmotor parkinsonian symptoms. Sci Adv *7*.
759 10.1126/sciadv.abd3994.
760 Dragicevic, E., Schiemann, J., and Liss, B. (2015). Dopamine midbrain neurons in health and Parkinson's
761 disease: emerging roles of voltage-gated calcium channels and ATP-sensitive potassium channels.
762 Neuroscience *284*, 798-814. 10.1016/j.neuroscience.2014.10.037.
763 Duzel, E., Bunzeck, N., Guitart-Masip, M., Wittmann, B., Schott, B.H., and Tobler, P.N. (2009).
764 Functional imaging of the human dopaminergic midbrain. Trends Neurosci *32*, 321-328.
765 10.1016/j.tins.2009.02.005.
766 Evans, R.C., Twedell, E.L., Zhu, M., Ascencio, J., Zhang, R., and Khaliq, Z.M. (2020). Functional
767 Dissection of Basal Ganglia Inhibitory Inputs onto Substantia Nigra Dopaminergic Neurons. Cell Rep
768 *32*, 108156. 10.1016/j.celrep.2020.108156.
769 Farassat, N., Costa, K.M., Stojanovic, S., Albert, S., Kovacheva, L., Shin, J., Egger, R., Somayaji, M.,
770 Duvarci, S., Schneider, G., and Roeper, J. (2019). In vivo functional diversity of midbrain dopamine
771 neurons within identified axonal projections. Elife *8*. 10.7554/eLife.48408.
772 Fieblinger, T., Zanetti, L., Sebastianutto, I., Breger, L.S., Quintino, L., Lockowandt, M., Lundberg, C., and
773 Cenci, M.A. (2018). Striatonigral neurons divide into two distinct morphological-physiological
774 phenotypes after chronic L-DOPA treatment in parkinsonian rats. Sci Rep *8*, 10068. 10.1038/s41598-
775 018-28273-5.
776 Gibb, W.R., and Lees, A.J. (1991). Anatomy, pigmentation, ventral and dorsal subpopulations of the
777 substantia nigra, and differential cell death in Parkinson's disease. J Neurol Neurosurg Psychiatry *54*,
778 388-396. 10.1136/jnnp.54.5.388.
779 Giguere, N., Burke Nanni, S., and Trudeau, L.E. (2018). On Cell Loss and Selective Vulnerability of
780 Neuronal Populations in Parkinson's Disease. Front Neurol *9*, 455. 10.3389/fneur.2018.00455.
781 Grace, A.A., and Bunney, B.S. (1984a). The control of firing pattern in nigral dopamine neurons: burst
782 firing. J Neurosci *4*, 2877-2890.
783 Grace, A.A., and Bunney, B.S. (1984b). The control of firing pattern in nigral dopamine neurons: single
784 spike firing. J Neurosci *4*, 2866-2876.
785 Gundersen, H.J. (1986). Stereology of arbitrary particles. A review of unbiased number and size
786 estimators and the presentation of some new ones, in memory of William R. Thompson. J Microsc
787 *143*, 3-45.
788 Guzman, J.N., Ilijic, E., Yang, B., Sanchez-Padilla, J., Wokosin, D., Galtieri, D., Kondapalli, J., Schumacker,
789 P.T., and Surmeier, D.J. (2018). Systemic isradipine treatment diminishes calcium-dependent
790 mitochondrial oxidant stress. J Clin Invest *128*, 2266-2280. 10.1172/JCI95898.
791 Heo, J.Y., Nam, M.H., Yoon, H.H., Kim, J., Hwang, Y.J., Won, W., Woo, D.H., Lee, J.A., Park, H.J., Jo, S.,
792 et al. (2020). Aberrant Tonic Inhibition of Dopaminergic Neuronal Activity Causes Motor Symptoms in
793 Animal Models of Parkinson's Disease. Curr Biol *30*, 276-291.e279. 10.1016/j.cub.2019.11.079.

Heymann, G., Jo, Y.S., Reichard, K.L., McFarland, N., Chavkin, C., Palmiter, R.D., Soden, M.E., and Zweifel, L.S. (2020). Synergy of Distinct Dopamine Projection Populations in Behavioral Reinforcement. Neuron *105*, 909-920 e905. 10.1016/j.neuron.2019.11.024.

Hollerman, J.R., and Grace, A.A. (1990). The effects of dopamine-depleting brain lesions on the electrophysiological activity of rat substantia nigra dopamine neurons. Brain Res *533*, 203-212. 10.1016/0006-8993(90)91341-d.

Kalia, L.V., and Lang, A.E. (2015). Parkinson's disease. Lancet *386*, 896-912. 10.1016/S0140-6736(14)61393-3.

Ketzef, M., Spigolon, G., Johansson, Y., Bonito-Oliva, A., Fisone, G., and Silberberg, G. (2017). Dopamine Depletion Impairs Bilateral Sensory Processing in the Striatum in a Pathway-Dependent Manner. Neuron *94*, 855-865 e855. 10.1016/j.neuron.2017.05.004.

Khaliq, Z.M., and Bean, B.P. (2008). Dynamic, nonlinear feedback regulation of slow pacemaking by A-type potassium current in ventral tegmental area neurons. J Neurosci *28*, 10905-10917. 10.1523/JNEUROSCI.2237-08.2008.

Kirik, D., Rosenblad, C., and Bjorklund, A. (1998). Characterization of behavioral and neurodegenerative changes following partial lesions of the nigrostriatal dopamine system induced by intrastriatal 6-hydroxydopamine in the rat. Exp Neurol *152*, 259-277. 10.1006/exnr.1998.6848.

Kordower, J.H., Olanow, C.W., Dodiya, H.B., Chu, Y., Beach, T.G., Adler, C.H., Halliday, G.M., and Bartus, R.T. (2013). Disease duration and the integrity of the nigrostriatal system in Parkinson's disease. Brain *136*, 2419-2431. 10.1093/brain/awt192.

Kravitz, A.V., Freeze, B.S., Parker, P.R., Kay, K., Thwin, M.T., Deisseroth, K., and Kreitzer, A.C. (2010). Regulation of parkinsonian motor behaviours by optogenetic control of basal ganglia circuitry. Nature *466*, 622-626. 10.1038/nature09159.

Liss, B., Franz, O., Sewing, S., Bruns, R., Neuhoff, H., and Roeper, J. (2001). Tuning pacemaker frequency of individual dopaminergic neurons by Kv4.3L and KChip3.1 transcription. EMBO J *20*, 5715-5724. 10.1093/emboj/20.20.5715.

Liss, B., and Striessnig, J. (2019). The Potential of L-Type Calcium Channels as a Drug Target for Neuroprotective Therapy in Parkinson's Disease. Annu Rev Pharmacol Toxicol *59*, 263-289. 10.1146/annurev-pharmtox-010818-021214.

McCutcheon, R.A., Abi-Dargham, A., and Howes, O.D. (2019). Schizophrenia, Dopamine and the Striatum: From Biology to Symptoms. Trends Neurosci *42*, 205-220. 10.1016/j.tins.2018.12.004.

Milosevic, L., Kalia, S.K., Hodaie, M., Lozano, A.M., Fasano, A., Popovic, M.R., and Hutchison, W.D. (2018). Neuronal inhibition and synaptic plasticity of basal ganglia neurons in Parkinson's disease. Brain *141*, 177-190. 10.1093/brain/awx296.

Ortner, N.J. (2021). Voltage-Gated Ca(2+) Channels in Dopaminergic Substantia Nigra Neurons: Therapeutic Targets for Neuroprotection in Parkinson's Disease? Front Synaptic Neurosci *13*, 636103. 10.3389/fnsyn.2021.636103.

Ortner, N.J., Bock, G., Dougalis, A., Kharitonova, M., Duda, J., Hess, S., Tuluc, P., Pomberger, T., Stefanova, N., Pitterl, F., et al. (2017). Lower Affinity of Isradipine for L-Type Ca(2+) Channels during Substantia Nigra Dopamine Neuron-Like Activity: Implications for Neuroprotection in Parkinson's Disease. J Neurosci *37*, 6761-6777. 10.1523/JNEUROSCI.2946-16.2017.

Otomo, K., Perkins, J., Kulkarni, A., Stojanovic, S., Roeper, J., and Paladini, C.A. (2020). In vivo patch-clamp recordings reveal distinct subthreshold signatures and threshold dynamics of midbrain dopamine neurons. Nat Commun *11*, 6286. 10.1038/s41467-020-20041-2.

Parker, J.G., Marshall, J.D., Ahanonu, B., Wu, Y.W., Kim, T.H., Grewe, B.F., Zhang, Y., Li, J.Z., Ding, J.B., Ehlers, M.D., and Schnitzer, M.J. (2018). Diametric neural ensemble dynamics in parkinsonian and dyskinetic states. Nature *557*, 177-182. 10.1038/s41586-018-0090-6.

Parker, P.R., Lalive, A.L., and Kreitzer, A.C. (2016). Pathway-Specific Remodeling of Thalamostriatal Synapses in Parkinsonian Mice. Neuron *89*, 734-740. 10.1016/j.neuron.2015.12.038.

Parkinson Study Group, S.-P.D.I.I.I.I. (2020). Isradipine Versus Placebo in Early Parkinson Disease: A Randomized Trial. Ann Intern Med *172*, 591-598. 10.7326/M19-2534.

Phillips, R.S., Rosner, I., Gittis, A.H., and Rubin, J.E. (2020). The effects of chloride dynamics on substantia nigra pars reticulata responses to pallidal and striatal inputs. Elife *9*. 10.7554/eLife.55592.

Pinault, D. (1996). A novel single-cell staining procedure performed in vivo under electrophysiological control: morpho-functional features of juxtacellularly labeled thalamic cells and other central neurons with biocytin or Neurobiotin. J Neurosci Methods *65*, 113-136. 10.1016/0165-0270(95)00144-1.

Poewe, W., Seppi, K., Tanner, C.M., Halliday, G.M., Brundin, P., Volkmann, J., Schrag, A.E., and Lang, A.E. (2017). Parkinson disease. Nat Rev Dis Primers *3*, 17013. 10.1038/nrdp.2017.13.

Poulin, J.F., Caronia, G., Hofer, C., Cui, Q., Helm, B., Ramakrishnan, C., Chan, C.S., Dombeck, D.A., Deisseroth, K., and Awatramani, R. (2018). Mapping projections of molecularly defined dopamine neuron subtypes using intersectional genetic approaches. Nat Neurosci *21*, 1260-1271. 10.1038/s41593-018-0203-4.

Poulin, J.F., Gaertner, Z., Moreno-Ramos, O.A., and Awatramani, R. (2020). Classification of Midbrain Dopamine Neurons Using Single-Cell Gene Expression Profiling Approaches. Trends Neurosci *43*, 155-169. 10.1016/j.tins.2020.01.004.

Rubi, L., and Fritschy, J.M. (2020). Increased GABAergic transmission in neuropeptide Y-expressing neurons in the dopamine-depleted murine striatum. J Neurophysiol *123*, 1496-1503. 10.1152/jn.00059.2020.

Saunders, A., Macosko, E.Z., Wysoker, A., Goldman, M., Krienen, F.M., de Rivera, H., Bien, E., Baum, M., Bortolin, L., Wang, S., et al. (2018). Molecular Diversity and Specializations among the Cells of the Adult Mouse Brain. Cell *174*, 1015-1030 e1016. 10.1016/j.cell.2018.07.028.

Schiemann, J., Schlaudraff, F., Klose, V., Bingmer, M., Seino, S., Magill, P.J., Zaghloul, K.A., Schneider, G., Liss, B., and Roeper, J. (2012). K-ATP channels in dopamine substantia nigra neurons control bursting and novelty-induced exploration. Nat Neurosci *15*, 1272-1280. 10.1038/nn.3185.

Schwarting, R.K., and Huston, J.P. (1996). The unilateral 6-hydroxydopamine lesion model in behavioral brain research. Analysis of functional deficits, recovery and treatments. Prog Neurobiol *50*, 275-331. 10.1016/s0301-0082(96)00040-8.

Sharott, A., Magill, P.J., Harnack, D., Kupsch, A., Meissner, W., and Brown, P. (2005). Dopamine depletion increases the power and coherence of beta-oscillations in the cerebral cortex and subthalamic nucleus of the awake rat. Eur J Neurosci *21*, 1413-1422. 10.1111/j.1460-9568.2005.03973.x.

Sitzia, G., Mantas, I., Zhang, X., Svenningsson, P., and Chergui, K. (2020). NMDA receptors are altered in the substantia nigra pars reticulata and their blockade ameliorates motor deficits in experimental parkinsonism. Neuropharmacology *174*, 108136. 10.1016/j.neuropharm.2020.108136.

Styr, B., Gonen, N., Zarhin, D., Ruggiero, A., Atsmon, R., Gazit, N., Braun, G., Frere, S., Vertkin, I., Shapira, I., et al. (2019). Mitochondrial Regulation of the Hippocampal Firing Rate Set Point and Seizure Susceptibility. Neuron *102*, 1009-1024 e1008. 10.1016/j.neuron.2019.03.045.

Subramaniam, M., Althof, D., Gispert, S., Schwenk, J., Auburger, G., Kulik, A., Fakler, B., and Roeper, J. (2014a). Mutant alpha-synuclein enhances firing frequencies in dopamine substantia nigra neurons by oxidative impairment of A-type potassium channels. J Neurosci *34*, 13586-13599. 10.1523/JNEUROSCI.5069-13.2014.

Surmeier, D.J. (2007). Calcium, ageing, and neuronal vulnerability in Parkinson's disease. Lancet Neurol *6*, 933-938. 10.1016/S1474-4422(07)70246-6.

Surmeier, D.J., Halliday, G.M., and Simuni, T. (2017a). Calcium, mitochondrial dysfunction and slowing the progression of Parkinson's disease. Exp Neurol *298*, 202-209. 10.1016/j.expneurol.2017.08.001.

Surmeier, D.J., Obeso, J.A., and Halliday, G.M. (2017b). Selective neuronal vulnerability in Parkinson disease. Nat Rev Neurosci *18*, 101-113. 10.1038/nrn.2016.178.

Tarfa, R.A., Evans, R.C., and Khaliq, Z.M. (2017). Enhanced Sensitivity to Hyperpolarizing Inhibition in Mesoaccumbal Relative to Nigrostriatal Dopamine Neuron Subpopulations. J Neurosci *37*, 3311-3330. 10.1523/JNEUROSCI.2969-16.2017.

Tinkhauser, G., Torrecillos, F., Pogosyan, A., Mostofi, A., Bange, M., Fischer, P., Tan, H., Hasegawa, H., Glaser, M., Muthuraman, M., et al. (2020). The Cumulative Effect of Transient Synchrony States on Motor Performance in Parkinson's Disease. J Neurosci *40*, 1571-1580. 10.1523/JNEUROSCI.1975-19.2019.

Turrigiano, G. (2012). Homeostatic synaptic plasticity: local and global mechanisms for stabilizing neuronal function. Cold Spring Harb Perspect Biol *4*, a005736. 10.1101/cshperspect.a005736.

Ungerstedt, U. (1968). 6-Hydroxy-dopamine induced degeneration of central monoamine neurons. Eur J Pharmacol *5*, 107-110. 10.1016/0014-2999(68)90164-7.

Ungless, M.A., and Grace, A.A. (2012). Are you or aren't you? Challenges associated with physiologically identifying dopamine neurons. Trends Neurosci *35*, 422-430. 10.1016/j.tins.2012.02.003.

West, T.O., Berthouze, L., Halliday, D.M., Litvak, V., Sharott, A., Magill, P.J., and Farmer, S.F. (2018). Propagation of beta/gamma rhythms in the cortico-basal ganglia circuits of the parkinsonian rat. J Neurophysiol *119*, 1608-1628. 10.1152/jn.00629.2017.

Wichmann, T., Bergman, H., and DeLong, M.R. (2018). Basal ganglia, movement disorders and deep brain stimulation: advances made through non-human primate research. J Neural Transm (Vienna) *125*, 419-430. 10.1007/s00702-017-1736-5.

Winkler, C., Kirik, D., Bjorklund, A., and Cenci, M.A. (2002). L-DOPA-induced dyskinesia in the intrastriatal 6-hydroxydopamine model of parkinson's disease: relation to motor and cellular parameters of nigrostriatal function. Neurobiol Dis *10*, 165-186. 10.1006/nbdi.2002.0499.

Zaghloul, K.A., Blanco, J.A., Weidemann, C.T., McGill, K., Jaggi, J.L., Baltuch, G.H., and Kahana, M.J. (2009). Human substantia nigra neurons encode unexpected financial rewards. Science *323*, 1496-1499. 10.1126/science.1167342.

Zhang, W., Xiong, B.R., Zhang, L.Q., Huang, X., Yuan, X., Tian, Y.K., and Tian, X.B. (2021). The Role of the GABAergic System in Diseases of the Central Nervous System. Neuroscience. 10.1016/j.neuroscience.2021.06.037.